

**Precise regional L5 positioning with IRNSS and QZSS
stand-alone and combined**

Wang, Kan; Chen, Pei; Zaminpardaz, Safoora; Teunissen, Peter J.G.

DOI

[10.1007/s10291-018-0800-4](https://doi.org/10.1007/s10291-018-0800-4)

Publication date

2019

Document Version

Final published version

Published in

GPS Solutions

Citation (APA)

Wang, K., Chen, P., Zaminpardaz, S., & Teunissen, P. J. G. (2019). Precise regional L5 positioning with IRNSS and QZSS: stand-alone and combined. *GPS Solutions*, 23(1), Article 10. <https://doi.org/10.1007/s10291-018-0800-4>

Important note

To cite this publication, please use the final published version (if applicable). Please check the document version above.

Copyright

Other than for strictly personal use, it is not permitted to download, forward or distribute the text or part of it, without the consent of the author(s) and/or copyright holder(s), unless the work is under an open content license such as Creative Commons.

Takedown policy

Please contact us and provide details if you believe this document breaches copyrights. We will remove access to the work immediately and investigate your claim.

Green Open Access added to TU Delft Institutional Repository

'You share, we take care!' – Taverne project

<https://www.openaccess.nl/en/you-share-we-take-care>

Otherwise as indicated in the copyright section: the publisher is the copyright holder of this work and the author uses the Dutch legislation to make this work public.



Precise regional L5 positioning with IRNSS and QZSS: stand-alone and combined

Kan Wang¹ · Pei Chen² · Safoora Zaminpardaz³ · Peter J. G. Teunissen^{1,4}

Received: 13 July 2018 / Accepted: 30 October 2018 / Published online: 10 November 2018
© Springer-Verlag GmbH Germany, part of Springer Nature 2018

Abstract

In this contribution we analyze the single-frequency L5 positioning capabilities of the two regional satellite navigation systems IRNSS and QZSS, stand alone as well as combined. The positioning analysis is done for two different baselines, having a mix of receivers, providing ambiguity-float and ambiguity-fixed positioning for models with and without zenith tropospheric delay (ZTD) estimation. The analyses include a precision analysis of the observed signals, as well as an analysis of the ambiguity resolution performance. This is done for both the multipath-uncorrected case as well as the multipath-mitigated case. It is shown that although single-system positioning performance is rather poor, the ZTD-fixed, single-epoch ambiguity success rates (ASRs) are close to 100% when the two regional systems are combined, thus providing mm-to-cm level precision for instantaneous ambiguity-fixed positioning. When the ZTD is estimated as well, only a few additional epochs are needed to get the ASRs close to 100%.

Keywords IRNSS · QZSS · Multipath · Ambiguity resolution · Ambiguity success-rate · L5 RTK positioning

Introduction

After the Japanese Quasi-Zenith Satellite System (QZSS) was realized as a four-satellite system in October 2017 (NSPS 2018a, b), the Indian Regional Navigation Satellite System (IRNSS), with the operational name of NavIC (Navigation with Indian Constellation), launched its eighth satellite in April 2018 (ISRO 2018). In addition to the first IRNSS satellite (IRNSS-1A), with failed onboard atomic clocks (<https://thewire.in/science/atomic-clock-rubidium-irNSS>) and located in inclined geosynchronous orbit (IGSO), there are four other IRNSS satellites located in the IGSO and another three in geostationary orbit (GEO), providing

standard positioning service (SPS) over the Indian landmass and Indian Ocean (Zaminpardaz et al. 2017). The L5 signal (1176.45 MHz) is shared by both the QZSS and IRNSS.

Australia benefits from the dual-system L5 signals. Figure 1 shows the ground tracks of the IRNSS and QZSS satellites based on the combined multi-GNSS Experiment (MGEX) broadcast ephemeris (BRDM 2018; Montenbruck et al. 2017) on Day of Year (DOY) 77, 2018, which does not contain the IRNSS satellite I01 with failed onboard clocks and the newly April launched I09. The details of the satellites are given in Table 1. The repeat cycles of the satellites from both systems amount to about 1 sidereal day, the patterns shown in Fig. 1 thus approximately repeat after about 23 h 56 min. The left and right panels of Fig. 2 illustrate the percentages within a 24 h period that at least 6 and 8 QZSS/IRNSS satellites are visible with an elevation angle above 10°, respectively, and the number of the QZSS/IRNSS satellites above the elevation mask as well as their sum for station CUT3 located in Perth, Australia. It can be observed that in a large part of Australia, at least 8 satellites can be observed during the entire day. In Perth, the number of the available satellites increases from about 4 in standalone cases to about 8 in combined case.

In recent years, several studies have been performed to analyze the signal characteristics of the IRNSS and QZSS

✉ Pei Chen
chenpei@buaa.edu.cn

¹ Department of Spatial Sciences, Curtin University, GPO Box U1987, Perth, WA 6845, Australia

² School of Astronautics, Beihang University, Beijing 100191, China

³ School of Science, College of Science, Engineering & Health, RMIT University, GPO Box 2476V, Melbourne, VIC 3001, Australia

⁴ Department of Geoscience and Remote Sensing, Delft University of Technology, 2628 CN Delft, The Netherlands

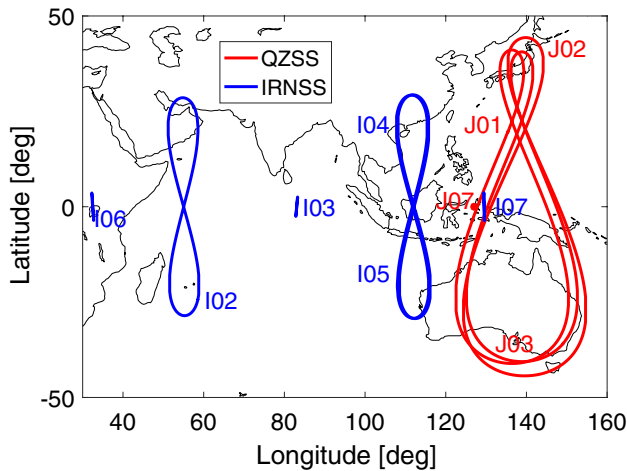


Fig. 1 Satellite ground tracks. The blue and red lines represent the ground tracks of the IRNSS and QZSS satellites, respectively. The plots were generated based on the combined multi-GNSS experiment (MGEX) broadcast ephemeris (BRDM 2018; Montenbruck et al. 2017) on DOY 77, 2018. Note that the IRNSS satellite I01 with failed onboard clocks and the newly launched I09 were not contained in the combined broadcast ephemeris on this day and are not shown in the plot

Table 1 Information of the QZSS and IRNSS satellites (MGEX 2017a, b; Zaminpardaz et al. 2017)

Satellite	PRN	Orbit type	Launch date
QZS-1 (Michibiki)	J01	QZO	September 2010
QZS-2 (Michibiki-2)	J02	QZO	June 2017
QZS-3 (Michibiki-3)	J07	GEO	August 2017
QZS-4 (Michibiki-4)	J03	QZO	October 2017
IRNSS-1A	I01	IGSO	July 2013
IRNSS-1B	I02	IGSO	April 2014
IRNSS-1C	I03	GEO	October 2014
IRNSS-1D	I04	IGSO	March 2015
IRNSS-1E	I05	IGSO	January 2016
IRNSS-1F	I06	GEO	March 2016
IRNSS-1G	I07	GEO	April 2016
IRNSS-1I	I09	IGSO	April 2018

signals (Hauschild et al. 2012; Nadarajah et al. 2016; Nie et al. 2015; Quan et al. 2016; Zaminpardaz et al. 2017, 2018). Zaminpardaz et al. (2017) gave both the undifferenced multipath-uncorrected and -corrected code and phase standard deviations in the zenith direction as well as the code-phase correlation coefficients for IRNSS and GPS L5 signals. For triple-frequency QZSS signals on L1, L2 and L5, Zaminpardaz et al. (2018) showed the undifferenced zenith-referenced standard deviations as well as the phase between-frequency covariances. It was verified that the

QZSS L5 code signals have higher precision than the L1 and L2 code signals before and after multipath corrections.

As stand-alone systems respectively, the real-time kinematic (RTK) positioning results were shown and discussed in Zaminpardaz et al. (2018) based on triple-frequency data from 4 QZSS satellites and in Zaminpardaz et al. (2016) using L5 signals from 6 IRNSS satellites. Combining QZSS satellites with other GNSS like GPS, Galileo and BDS, RTK results were also studied in Odolinski and Teunissen (2017), Odolinski et al. (2015). In Nadarajah et al. (2016), the L5 signals from IRNSS, GPS, Galileo and QZSS were combined for analysis of the RTK and attitude determination performances, however, based only on two IRNSS satellites (I01 and I02) and one QZSS satellite (J01). As the number of satellites of both the IRNSS and QZSS has largely increased during recent years, taking advantage of Australia’s location, it is now possible to assess the ambiguity resolution and positioning performances using the QZSS/IRNSS combined L5 signals with more satellites (see Fig. 2).

This contribution thus aims to study the potential of single-frequency L5 RTK positioning using the two regional satellite systems. We first introduce our observational model and then perform a signal analysis of the QZSS and IRNSS L5-code and -phase data for both the multipath-uncorrected and -corrected cases. This is followed by our ambiguity resolution and positioning analyses, first of a short baseline using identical receivers and no atmospheric delays, and then of a longer baseline, using mixed receivers. Our study includes both formal and empirical analyses of the ambiguity success rates (ASRs) and positioning precision.

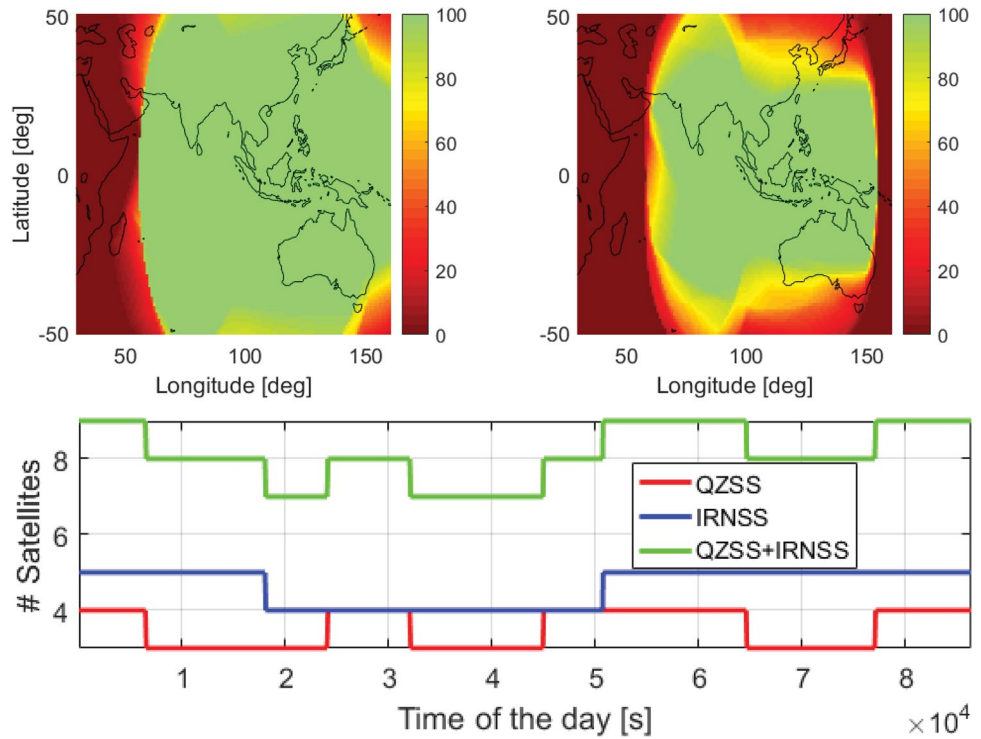
Processing strategy

For a single-frequency model, the expectation of the double-differenced (DD) observed-minus-computed (O – C) terms of the code Δp and phase observations $\Delta \phi$ of a single baseline can be formulated as (Teunissen and Montenbruck 2017):

$$E \begin{bmatrix} \Delta p \\ \Delta \phi \end{bmatrix} = \begin{bmatrix} D_m^T G & 0 \\ D_m^T G & \lambda_j I_{m-1} \end{bmatrix} \begin{bmatrix} \Delta \rho \\ a \end{bmatrix} \tag{1}$$

with $E[\cdot]$ denoting the expectation operator. The matrix D_m^T is the differencing operator given as $D_m^T = [-e_{m-1}, I_{m-1}]$, where m denotes the number of satellites. The term I_{m-1} denotes the identity matrix of size $m - 1$. The vector $\Delta \rho$ contains the geometry elements, i.e., the three-dimensional baseline increment Δx and, for baselines with a length of several kilometers, it may also contain the between-receiver zenith tropospheric delay (ZTD) increment $\Delta \tau$. The a priori tropospheric delays are computed with the Saastamoinen model (Saastamoinen 1972) and are corrected in the O – C terms. The matrix G is given as $G = [u^1, \dots, u^m]^T$, with u^s

Fig. 2 Percentage color maps and number of visible satellites. Percentages within a 24 h period that at least 6 (top left) and 8 (top right) QZSS/IRNSS satellites are simultaneously visible above the elevation mask of 10°, and the numbers of the QZSS and IRNSS satellites visible above the elevation mask as well as their sum for station CUT3 in Perth, Australia (bottom). The plots were generated based on the combined MGEX broadcast ephemeris (BRDM 2018; Montenbruck et al. 2017) on DOY 77, 2018. Note that the IRNSS satellite I01 with failed onboard clocks and the newly launched I09 were not contained in the combined broadcast ephemeris on this day and are not included in the plot. The colormaps in the top panel were generated based on a data sampling interval of 30 s



denoting the satellite-to-receiver unit vectors, and in case of the presence of $\Delta\tau$, $G = \begin{bmatrix} [u^1, \dots, u^m]^T, [g^1, \dots, g^m]^T \end{bmatrix}$, with g^s denoting the elevation-dependent tropospheric mapping function, here the Ifadis mapping function (Ifadis 1986). For baselines within 10 km, we assume the tropospheric mapping functions of both receivers g_1^s and g_2^s to be the same, and therefore, we drop their subscript. The vector a represents the DD ambiguities in cycles, and λ_j denotes the wavelength of the frequency used for the processing, i.e., L5. We remark that for each epoch, we select only one reference satellite and thus not a system-specific reference satellite. By forming between-system double differences, we assume the differential inter-system biases (ISBs) to be zero for baselines with the same receiver and antenna types (Odijk et al. 2017). For baselines with mixed receiver types, the processing is only performed in multipath-mitigated case, where the day-differenced observations are used. As the differential ISBs are assumed to be constant over two consecutive days, they are considered removed through multipath mitigation.

The dispersion of the DD O – C terms (1) is given as

$$D \begin{bmatrix} \Delta p \\ \Delta \phi \end{bmatrix} = \begin{bmatrix} D_m^T Q_p W^{-1} D_m & 0 \\ 0 & D_m^T Q_\phi W^{-1} D_m \end{bmatrix} \quad (2)$$

where the $m \times m$ diagonal matrices Q_p and Q_ϕ contain the undifferenced zenith-referenced variances on L5 code and phase observations, respectively, for satellites of the corresponding systems. $D[\cdot]$ denotes the dispersion operator, and the inversed between-receiver weight matrix W^{-1} is given as

$$W^{-1} = W_1^{-1} + W_2^{-1} = \text{diag}(w_1^1, \dots, w_1^m)^{-1} + \text{diag}(w_2^1, \dots, w_2^m)^{-1} \quad (3)$$

where $\text{diag}(\cdot)$ denotes the diagonal matrix with the diagonal elements contained in (\cdot) . The term w_r^s is the elevation-dependent exponential weighting function (Euler and Goad 1991):

$$w_r^s = \left(1 + 10 \exp\left(-\frac{e_r^s}{10}\right) \right)^{-2} \quad (4)$$

for which e_r^s denotes the elevation angle from receiver r to satellite s in degrees, and $\exp(\cdot)$ is the natural exponential function. In this study, the elevation mask is set to be 10°.

Measurement setup

In this study, the 1 Hz QZSS and IRNSS phase and code observations on L5 were collected from receivers CUT3, CUBB, CUCC located in Curtin University, Perth, Australia and UWA0 located at the University of Western Australia, Perth, Australia. The very short baseline CUT3–CUBB of around 4 m and the longer baseline CUCC–UWA0 of around 8 km (Fig. 3) were formed for the RTK processing. Receivers of the same type JAVAD TRE_G3TH DELTA and antennas of the same type TRM 59800.00 SCIS were used for the baseline CUT3–CUBB. For the baseline CUCC–UWA0, mixed receiver and antenna types were used as shown in Table 2.

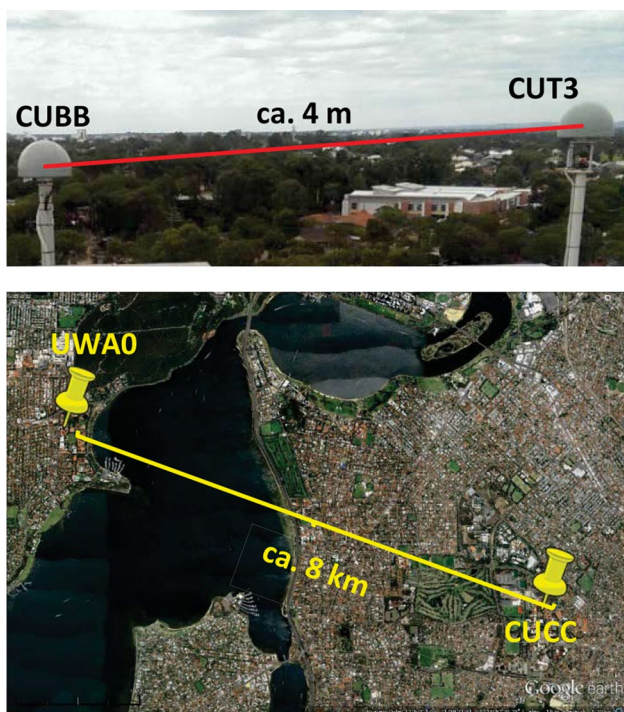


Fig. 3 Baselines used for the processing. The baseline CUT3–CUBB (top) of around 4 m and the baseline CUCC–UWA0 (bottom) of around 8 km are located in Perth, Australia. Map data (bottom) @ 2018 Google (Google Earth 2018)

Table 2 Receiver and antenna types of the stations used for the processing

Station	Receiver type	Antenna type
CUT3	JAVAD TRE_G3TH DELTA	TRM 59800.00 SCIS
CUBB		
CUCC		
UWA0	SEPT POLARX5	JAVRINGANT_DM SCIS

In this contribution, days in March/April 2018 were used for analysis of the signal characteristics and RTK processing. Figure 4 shows the skyplot of the IRNSS and QZSS satellites for the station CUT3 on DOY 77, 2018. The skyplot was generated based on the combined MGEX broadcast ephemeris on this day (BRDM 2018; Montenbruck et al. 2017).

Figure 5 shows the position dilution of precision (PDOP) of the baseline CUT3–CUBB for QZSS-standalone, IRNSS-standalone and QZSS/IRNSS-combined cases on DOY 77, 2018. The PDOP is calculated with:

$$PDOP = \sqrt{\frac{\text{tr}\left\{\left(G^T D_m W_{DD} D_m^T G\right)^{-1}\right\}}{2}} \quad (5)$$

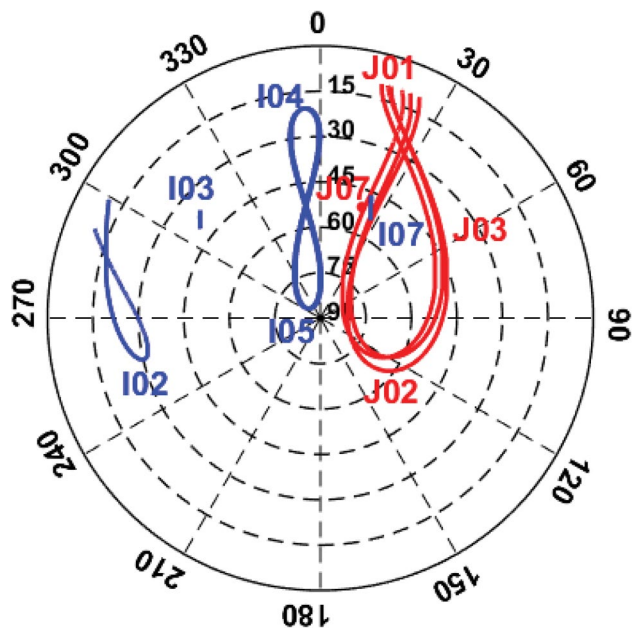


Fig. 4 Skyplot of the IRNSS and QZSS satellites. The blue and red lines represent the skyplots of the IRNSS and QZSS satellites for the station CUT3 on DOY 77, 2018, respectively. The plot was generated based on the ground truth of station CUT3 and the combined MGEX broadcast ephemeris (BRDM 2018; Montenbruck et al. 2017)

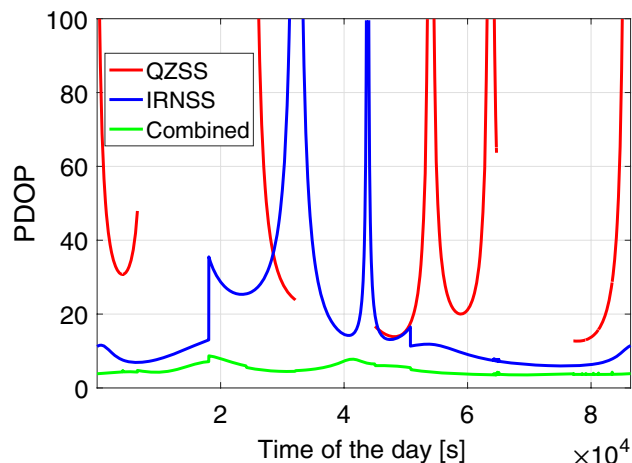


Fig. 5 PDOP time series. The baseline CUT3–CUBB on DOY 77, 2018 was used for computing the PDOPs in QZSS-standalone (red), IRNSS-standalone (blue) and QZSS/IRNSS-combined (green) cases

with

$$W_{DD} = \left(D_m^T W^{-1} D_m\right)^{-1} \quad (6)$$

where $\text{tr}\{\cdot\}$ denotes the trace of the matrix contained in $\{\cdot\}$. The term G contains here only the satellite-to-receiver unit vectors, and the inversed between-receiver weight matrix W^{-1} can be obtained with (3). We remark that the data used

in this study went through a screening process in the single point positioning (SPP) procedure and was afterwards checked for possible half cycle problems after cycle slips. Gaps in Fig. 5 are caused by time points with less than four satellites or with PDOPs larger than 100, which are not used in the processing. The maximal PDOP in the combined case is about 8.7.

Stochastic properties

In this section, the L5 code and phase signals are analyzed for QZSS and IRNSS satellites in multipath-uncorrected and -mitigated cases. The geometric ranges and the integer DD ambiguities are assumed known and removed from the DD observations so that the remaining DD residuals contain only the noise, multipath effects and for the baseline CUCC–UWA0 also the DD atmospheric delays:

$$\begin{bmatrix} e_p \\ e_\phi \end{bmatrix} = \begin{bmatrix} p \\ \phi \end{bmatrix} - \begin{bmatrix} I_{m-1} & 0 \\ I_{m-1} & \lambda_j I_{m-1} \end{bmatrix} \begin{bmatrix} \rho \\ a \end{bmatrix} \tag{7}$$

where e_p and e_ϕ represent the DD code and phase residuals, respectively, and p and ϕ stand for the DD code and phase observations, respectively. The vector ρ denotes the DD geometric ranges. For the 4 m baseline CUT3–CUBB, the ambiguities were obtained with the single-epoch baseline-known model, for which the DD geometric ranges computed from the ground truth were removed from the DD phase observations, and the DD ambiguities were obtained by rounding the residuals divided by the wavelength. For the 8 km baseline CUCC–UWA0, the referenced ambiguities were obtained with the stronger multi-epoch baseline-known model, for which the ambiguities are assumed to be constant in time. For multipath mitigation, the DD residuals on the subsequent day are subtracted from those on the processing day. A time shift of 4 min was considered by forming the day-to-day differences. Assuming that the satellite configuration approximately repeats on the subsequent day after shifting 4 min, the multipath is considered to be removed to a large extent. The remaining residuals contain thus for the 4 m baseline CUT3–CUBB mainly the noise, and for the 8 km baseline CUCC–UWA0 mainly the noise and the day-to-day DD atmospheric delays. Figure 6 shows the time correlation for the baseline CUT3–CUBB using 1 h data on DOY 75, 2018. The data on DOY 76 was used for multipath mitigation. The figures illustrate the influence of the multipath mitigation procedure on the time correlation of the observations. The large correlations were reduced to ignorable level after mitigating the multipath.

Using the least-squares variance component estimation (LS-VCE) procedure (Amiri-Simkooei et al. 2009; Teunissen and Amiri-Simkooei 2008), the undifferenced standard

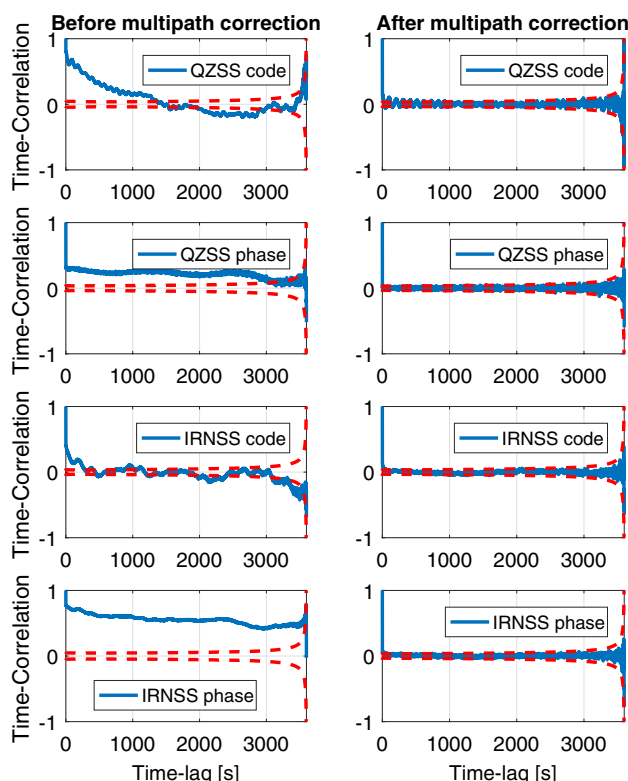


Fig. 6 Time correlation of the L5 signals of baseline CUT3-CUBB. The code and phase signals from QZSS and IRNSS satellites from 00:04:00 to 01:03:59 in GPS time (GPST) on DOY 75, 2018 were used for the plots before (left) and after multipath mitigation (right). Data from 00:00:00 to 00:59:59 in GPST on DOY 76 of 2018 was used for multipath mitigation

deviations were computed in the zenith direction for L5 code and phase signals of QZSS and IRNSS separately. For the 4 m baseline CUT3–CUBB, time points on DOY 75 and 76 (shifted by 4 min for multipath mitigation) with observations from 4 QZSS satellites (J01, J02, J03, J07) and 5 IRNSS satellites (I02, I03, I04, I05, I07) were used for signal analysis of QZSS and IRNSS, respectively. For the 8 km baseline CUCC–UWA0, the data on DOY 70 and 71 was used for signal analysis in the multipath-mitigated case. We note that by forming geometry-free combination using L1 and L5 phase signals of the QZSS satellites, the ionospheric behaviors for the QZSS satellites during the time epochs used for signal analysis on DOY 70 and 71 for baseline CUCC–UWA0 are mostly shown to be quiet. We thus ignored the DD ionospheric delays for the 8 km baseline but considered only its DD ZTDs. For the baseline CUCC–UWA0, the standard deviations for QZSS L5 signals were taken from Zaminpardaz et al. (2018), and those for L5 IRNSS signals were calculated in multipath-mitigated case. We remark that after multipath mitigation, the factor of $\sqrt{2}$ caused by forming day-to-day differences are included in the third and fourth columns. For the short baseline CUT3–CUBB, the signal standard deviations of QZSS and

IRNSS are found to be similar to those performed for other short baselines of the same receiver/antenna type in Zaminpardaz et al. (2017, 2018), when the factor of $\sqrt{2}$ is correctly considered. The correlation coefficients between L1/L2/L5 QZSS phase signals are found to be small in Zaminpardaz et al. (2018), and are not considered in this study.

From Table 3, for the baseline CUT3–CUBB, we see that even with the enlarged noise by forming day-to-day differences considered in the multipath-mitigated case, the standard deviations after multipath mitigation are similar to or smaller than those before multipath mitigation. The QZSS L5 code signal is shown to be more precise than the IRNSS L5 code signal.

Baseline CUT3–CUBB

In this section, the ambiguity resolution and RTK positioning performance of the 4 m baseline CUT3–CUBB are analyzed assuming that the DD atmospheric delays are negligible. It is based on single-epoch processing using all the four QZSS satellites and five IRNSS satellites (I02, I03, I04, I05, I07) with observations available on the processing day and the subsequent day shifted by 4 min for multipath mitigation. Time epochs with PDOP larger than 100 are excluded from the analysis.

Ambiguity resolution

Making use of the variance matrix of the float ambiguities $Q_{\hat{a}\hat{a}}$, the ambiguity dilution of precision (ADOP) measures the model strength for ambiguity resolution (Teunissen 1997) with:

$$ADOP = \sqrt{|Q_{\hat{a}\hat{a}}|}^{\frac{1}{m-1}} \tag{8}$$

where $|\cdot|$ denotes the determinant of the corresponding matrix. Using the time points explained above for the processing day DOY 77, 2018, the ADOP values are shown in Fig. 7 for the multipath-uncorrected case. The black dashed line marks the ADOP of 0.12 cycles, which as a rule of thumb corresponds to an integer least-squares (ILS) ASR of 99.9% (Odijk and Teunissen 2008). The gaps in the red

line correspond to the time points with PDOP larger than 100, which are not used in further data analysis. We see that combining both systems is helpful to improve the ambiguity resolution. The green line is below 0.12 cycles, which indicates an ILS ASR higher than 99.9% in combined case. Note that the integer bootstrapping (IB) ASR that is used in this paper lower bounds the ILS ASR (Teunissen 1999).

Using the time points shown in Fig. 7, after decorrelation of the variance–covariance matrix of the float ambiguities, the formal integer bootstrapping (IB) ASR P_F is computed for each epoch as (Teunissen 1998):

$$P_F = \prod_{i=1}^{m-1} \left(2\Phi\left(\frac{1}{2\sigma_{\hat{a}_i}}\right) - 1 \right) \tag{9}$$

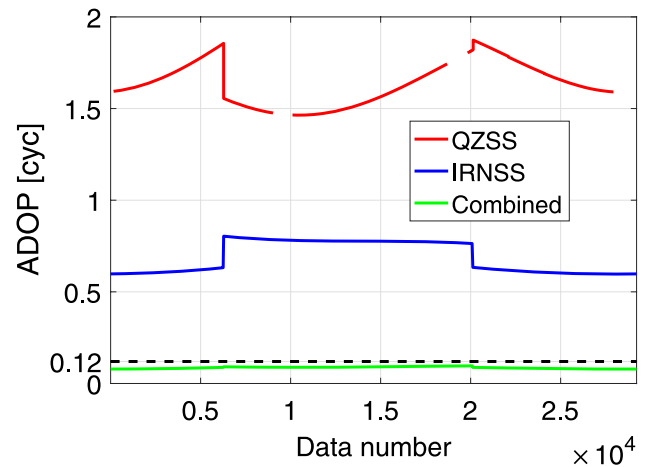


Fig. 7 L5 ADOP time series. Results are illustrated for the QZSS-standalone (red), IRNSS-standalone (blue) and QZSS/IRNSS-combined (green) cases for the baseline CUT3–CUBB using multipath-uncorrected observations on DOY 77, 2018. The time points used in the plot have simultaneously observations from 4 QZSS and 5 IRNSS satellites (I02, I03, I04, I05, I07) on DOY 77 and 78 (shifted by 4 min). The gaps in the red line represent the time points with PDOP larger than 100. The black dashed line marks the ADOP of 0.12 cycles

Table 3 Zenith-referenced standard deviations for undifferenced L5 code and phase observations of QZSS and IRNSS satellites

	CUT3–CUBB (4 m)		CUCC–UWA0 (8 km)
	MP-uncorrected	MP-mitigated	MP-mitigated
QZSS L5 code (m)	0.16	0.11	0.08
QZSS L5 phase (m)	0.002	0.002	0.003
IRNSS L5 code (m)	0.27	0.28	0.21
IRNSS L5 phase (m)	0.002	0.001	0.003

Data on DOY 75 and 70, 2018 was used for the signal analysis of the baseline CUT3–CUBB and CUCC–UWA0, respectively. Data on DOY 76 and 71, 2018 was used for multipath mitigation. We remark that after multipath mitigation, the factor of $\sqrt{2}$ caused by forming day-to-day differences are included in the third and fourth columns. The QZSS standard deviations for baseline CUCC–UWA0 were taken from Zaminpardaz et al. (2018)

with

$$\Phi(x) = \int_{-\infty}^x \frac{1}{\sqrt{2\pi}} \exp\left(-\frac{u^2}{2}\right) du \tag{10}$$

where $\sigma_{\hat{a}_{i|l}}$ represents the conditional standard deviation of the i -th decorrelated ambiguity with $l = 1, \dots, i - 1$. The average formal ASRs are then compared with the empirical IB success rates P_E of the multipath-uncorrected and -mitigated cases, computed as

$$P_E = \frac{N_C}{N} \tag{11}$$

where N_C and N represent the number of epochs with correctly fixed ambiguities and the number of all processing epochs, respectively. The reference ambiguities were obtained with the single-epoch baseline-known model. The comparison is performed for QZSS-standalone, IRNSS-standalone and QZSS/IRNSS-combined cases and shown in Table 4. Compared to the standalone cases, both the formal and empirical ASRs increase from below 10% to almost 100%. The empirical and formal success rates correspond mostly well with each other, which indicates the correspondence of the model with the data. Note that the values given in Table 4 only intends to provide an overview of the ASRs with the best satellite configurations that can be achieved on the test day for the very short baseline in Perth, i.e., at the time points with 4 QZSS and 5 IRNSS satellites available.

Positioning performance

Making use of the L5 signals from the four QZSS satellites J01, J02, J03 and J07, as well as the five IRNSS satellites I02, I03, I04, I05 and I07 as shown in Fig. 4, the RTK positioning performance is evaluated for the 4 m baseline CUT3–CUBB in QZSS/IRNSS standalone cases and combined case. The time points on DOY 77, 2018 as shown in Fig. 7 were used for the data analysis. The data on DOY 78, 2018 was used for multipath mitigation.

Table 4 Single-epoch empirical and average formal ASRs (see 9, 11)

	MP-uncorrected		MP-mitigated	
	Empirical	Formal	Empirical	Formal
QZSS	0.019	0.014	0.058	0.036
IRNSS	0.069	0.080	0.096	0.091
QZSS/IRNSS	0.997	1.000	0.997	1.000

The results are given for the QZSS/IRNSS-standalone and -combined cases. The same time points on DOY 77, 2018 were used as in Fig. 7. Data on DOY 78 was used for multipath mitigation

Using only QZSS or IRNSS satellites, the single-epoch L5 positioning results are of poor precision. Due to the low ASRs, as shown in Table 4, only the float north, east and height baseline errors are plotted in Fig. 8 for the multipath-mitigated case using the QZSS satellites (left) and IRNSS satellites (right), respectively. It can be observed that the float solutions are in the range of tens of meters. For reason of comparison, the y-axis of the east errors is scaled to 50 m. For IRNSS-standalone solutions, the meter-level east errors are smaller than those in the other two directions. As explained in Zaminpardaz et al. (2018), in single-system single-epoch case, the precision of the north, east and height baseline increments is related to the components in $\left|\sqrt{w^s(u^s - \bar{u})}\right|$, with the assumption that $w_1^s \approx w_2^s$ for the 4 m baseline and the subscripts are thus dropped. The term \bar{u} is equal to $\sum_{s=1}^m (w^s u^s) / \sum_{s=1}^m w^s$. A larger component in $\left|\sqrt{w^s(u^s - \bar{u})}\right|$ leads to a better precision of the corresponding baseline increments. The small east errors in IRNSS-standalone case (right panel of Fig. 8) can thus be explained by Fig. 9. From Fig. 8 we can also observe a poorer precision of the east baseline estimates in QZSS-standalone case than that of the other two directions (left panel of Fig. 8). This corresponds to the results in Zaminpardaz et al. (2018) and are not explained here again.

After combining both systems, the error ranges are reduced in all the three directions. Figure 10 illustrates the north, east and height errors of the same baseline in QZSS/IRNSS-combined case. The gray, green and red dots correspond to the ambiguity-float, ambiguity-correctly-fixed, and ambiguity-wrongly-fixed cases, and the blue line represents the 95% confidence intervals of the float solutions. We see that the large systematic effects in the multipath-uncorrected case are reduced after multipath mitigation. This is directly reflected in the reduced mean values in the absolute sense as shown in Table 5. We remark that in Table 5 only the time points with correctly fixed ambiguities were used to calculate the mean values in ambiguity-fixed case. The ambiguity-fixed mean values are not given for the standalone cases since they are not considered representative with the low ASRs shown in Table 5. After multipath mitigation, the percentage of float solutions (gray dots) within the 95% formal confidence intervals (blue lines) is around 96.3%, 95.6% and 93.1% in the north, east and up directions, respectively. This shows the correspondence between the formal and empirical solutions.

The empirical and average formal standard deviations of the north, east and height errors are shown in Table 6 in multipath-uncorrected and -mitigated cases. We remark that only the time points with correctly-fixed ambiguities were used for computing the standard deviations in ambiguity-fixed case, and the average formal standard deviations are

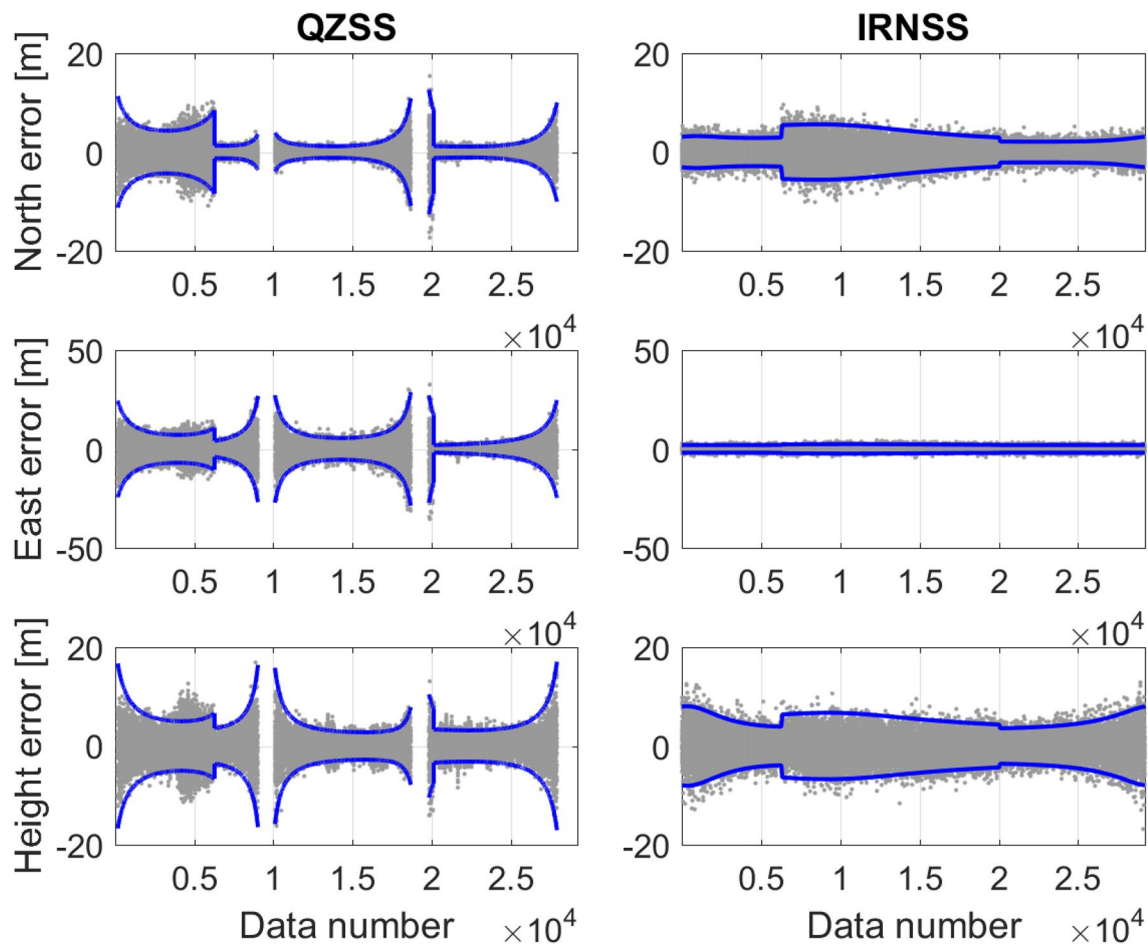


Fig. 8 North, east and height baseline errors in QZSS/IRNSS-standalone case. The gray dots represent the ambiguity-float solutions for the baseline CUT3–CUBB in QZSS-standalone (left) and IRNSS-standalone cases (right) after multipath mitigation, and the blue lines represent the 95% formal confidence intervals of the float solutions.

The same time points on DOY 77, 2018 were used as in Fig. 7. Data on DOY 78, 2018 was used for multipath mitigation. The gaps in the left panel represent the time points with PDOP larger than 100, which are not used in the data analysis

calculated as the square roots of the mean formal variances. Due to the low ASRs in QZSS/IRNSS-standalone cases (Table 5), their standard deviations in the ambiguity-fixed case are not considered representative and are not given in the table. Using QZSS/IRNSS-combined observations, the standard deviations are within decimeters and millimeters in ambiguity-float and -fixed cases, respectively. In ambiguity-float case, the standard deviations are reduced from meters in standalone cases to decimeters in QZSS/IRNSS-combined case. Note the correspondence between the empirical and formal results.

To have an overview of the GPS-related single-epoch RTK performance in Perth, in Table 7 we also give the daily mean formal ASRs and formal standard deviations of the positioning errors in L5 single-, dual- and triple-system cases for baseline CUT3–CUBB. The satellite configurations on DOY 77, 2018, the ground truth of the baselines, and the multipath-mitigated standard deviations given in Table 3

were used for the processing. The GPS L5 code and phase multipath-mitigated standard deviations were taken from Zaminpardaz et al. (2017), and the sampling rate is 1 Hz. All time epochs with not less than 4 satellites above the elevation mask and with PDOP smaller than 100 were used for the processing. The percentage of these epochs within one day is denoted by $p_{s \geq 4}$. Note that the results shown in Table 7 is purely based on geometry and is not related to any real observations. Only the time points with ASR larger than 99.9% were used for computing the ambiguity-fixed standard deviations. As shown in the second column of Table 7, the number of time points that was taken into account for calculating the mean ASRs and standard deviations are different for different system combinations. The mean formal ASR of about 0.285 in GPS-standalone case, e.g., was computed based on about 44% of the time points in the test day. In other time points, the number of the available GPS IIF satellites is mostly lower than that of the IRNSS satellites,

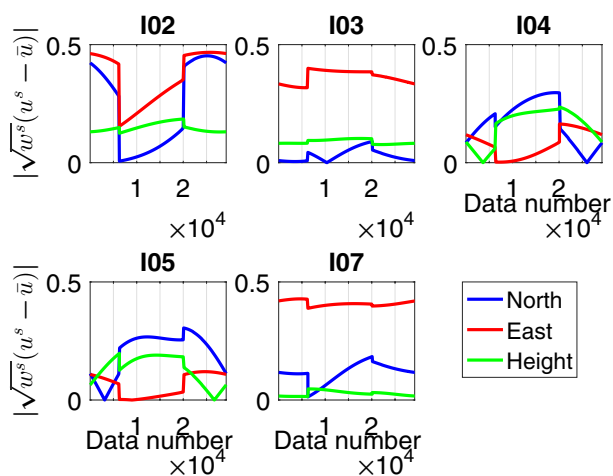


Fig. 9 Absolute values of the components in $\sqrt{w^s(u^s - \bar{u})}$ for IRNSS satellites. The values are computed for the baseline CUT3–CUBB in the IRNSS-standalone case after multipath mitigation. The same time points on DOY 77, 2018 were used as in Fig. 7

which results in a lower mean formal ASR in QZSS/GPS-combined case than that in QZSS/IRNSS-combined case. Within several hours, only one or two GPS IIF satellites are above the elevation mask. This results in low ASRs in, e.g., IRNSS/GPS-combined case during these time periods, and slightly lower mean formal ASRs in IRNSS/GPS-combined case than that in QZSS/IRNSS-combined case.

From Table 7 it can be observed that low daily mean ASRs of single-epoch L5 QZSS/IRNSS/GPS-standalone solutions increase to above 85% after using combined observations from any two systems. Among them, the QZSS/IRNSS, IRNSS/GPS and QZSS/IRNSS/GPS-combined solutions have reached a daily mean ASR of above 95%. Millimeter-level ambiguity-fixed standard deviations can be obtained for the combined cases using time epochs with ASRs larger than 99.9%.

Apart from for the 4 m baseline in Perth, we also computed the daily average formal standard deviations of the north, east and height errors for short baselines located in a larger area, including part of the QZSS and IRNSS service areas. The results are processed in the QZSS/IRNSS-combined case using multipath-mitigated signal standard

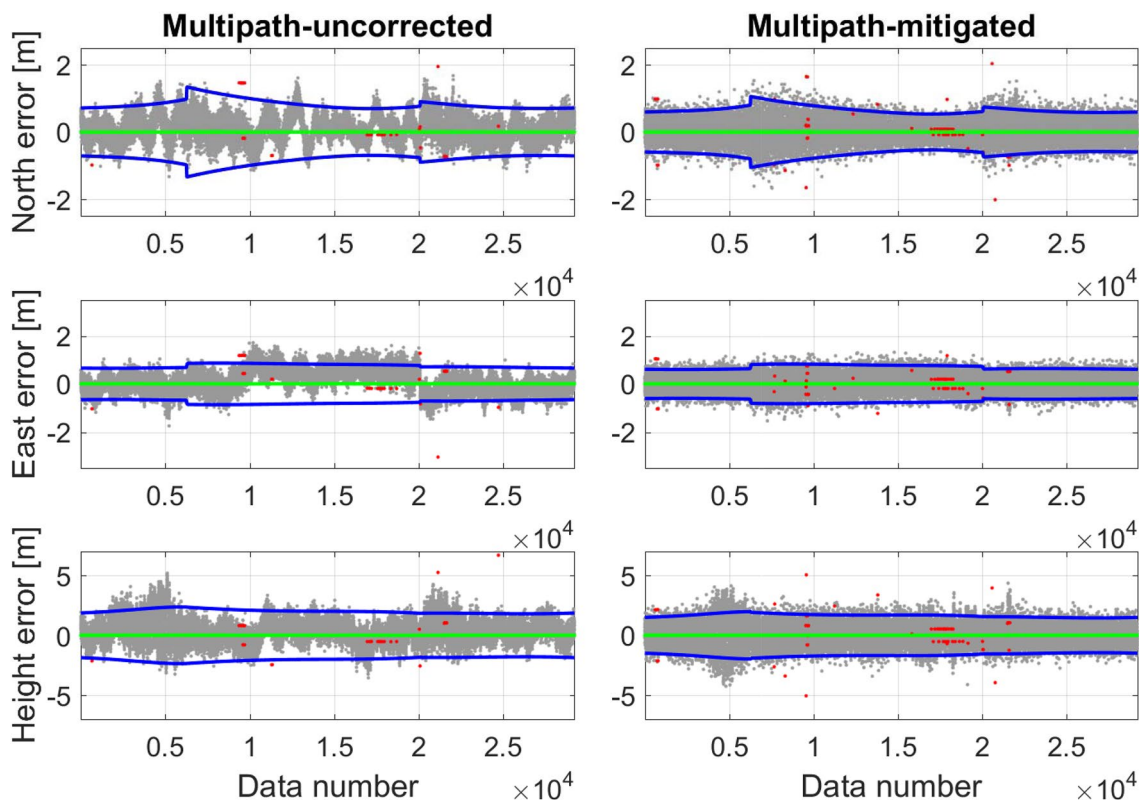


Fig. 10 North, east and height baseline errors in QZSS/IRNSS-combined case. The gray, green and red dots represent the ambiguity-float, ambiguity-correctly-fixed and ambiguity-wrongly-fixed solutions, respectively, before (left) and after multipath mitigation (right) for baseline CUT3–CUBB. The blue lines represent the 95% formal

confidence intervals of the float solutions. The processing is based on QZSS/IRNSS-combined L5 observations with the same time points on DOY 77, 2018 used as in Fig. 7. Data on DOY 78, 2018 was used for multipath mitigation

Table 5 Mean of the single-epoch positioning errors

Direction	Ambiguity float (m)		Ambiguity-fixed (m)	
	MP-uncorrected	MP-mitigated	MP-uncorrected	MP-mitigated
North	0.07/−0.44/0.09	−0.03/0.09/0.03	−/−/−0.001	−/−/−0.000
East	−0.33/0.36/0.11	−0.17/0.10/0.02	−/−/0.003	−/−/0.000
Height	0.66/−0.73/0.34	−0.00/−0.11/0.06	−/−/0.000	−/−/0.000

The results are given in the format of the QZSS-standalone/IRNSS-standalone/QZSS-IRNSS-combined cases. The same time points on DOY 77, 2018 were used as in Fig. 7. Data on DOY 78, 2018 was used for multipath mitigation

Table 6 Empirical and average formal standard deviations of the single-epoch positioning errors

System	Direction	Ambiguity float (m)		Ambiguity-fixed (m)	
		MP-uncorrected	MP-mitigated	MP-uncorrected	MP-mitigated
QZSS	North	2.35 (2.67)	1.76 (1.93)	−	−
	East	5.47 (6.79)	4.18 (4.90)	−	−
	Height	4.09 (4.13)	2.68 (2.98)	−	−
IRNSS	North	2.12 (1.88)	1.85 (1.89)	−	−
	East	1.41 (1.07)	1.07 (1.08)	−	−
	Height	2.83 (2.85)	2.60 (2.86)	−	−
QZSS/IRNSS	North	0.37 (0.43)	0.32 (0.34)	0.003 (0.004)	0.003 (0.004)
	East	0.48 (0.39)	0.35 (0.36)	0.002 (0.003)	0.003 (0.003)
	Height	0.98 (1.02)	0.93 (0.84)	0.007 (0.008)	0.006 (0.008)

The results are presented for the baseline CUT3-CUBB with the formal results given in brackets. The same time points on DOY 77, 2018 were used as in Fig. 7. Data on DOY 78, 2018 was used for multipath mitigation

Table 7 Daily average formal RTK solutions for the baseline CUT3-CUBB

System	$p_{s \geq 4}$ (%)	\bar{P}_F	Ambiguity-float (m)			Ambiguity-fixed (m)		
			North	East	Height	North	East	Height
QZSS	43	0.032	1.74	4.78	2.82	−	−	−
IRNSS	97	0.056	4.57	1.66	6.39	−	−	−
GPS	44	0.285	0.96	0.43	1.22	−	−	−
QZSS/IRNSS	100	0.995	0.54	0.40	1.06	0.005	0.003	0.009
QZSS/GPS	100	0.871	0.28	0.56	0.75	0.003	0.003	0.007
IRNSS/GPS	100	0.966	0.35	0.43	1.01	0.002	0.003	0.006
QZSS/IRNSS/GPS	100	1.000	0.20	0.23	0.54	0.002	0.002	0.006

All time epochs on DOY 77, 2018 with not less than 4 satellites above the elevation mask and with PDOP smaller than 100 were used for processing. The terms $p_{s \geq 4}$ and \bar{P}_F denote the percentage of these epochs within the test day and the mean formal ASR, respectively. The analysis was performed using multipath-mitigated signal standard deviations. Note that the ambiguity-fixed standard deviations are computed only based on the time epochs with ASR larger than 99.9%. The GPS IIF satellites sending L5 signals were used for computation of the GPS-related cases

deviations. The reference stations are assumed to be located at the grid points from 35°S to 30°N with a step of 5° in latitude and from 70°E to 145°E with a step of 5° in longitude. All time points on DOY 77, 2018 with at least 4 satellites above the elevation mask and with PDOP smaller than 100 were used for the analysis. Only the time epochs with the ASR larger than 99.9% were used to compute the ambiguity-fixed solutions. The grid values are smoothed in

Fig. 11 for visualization purpose. As shown in the figure, in the north-west of Australia, the average formal standard deviations of the positioning errors amount to about 4 and 8 dm in the horizontal (north and east) and vertical directions, respectively, in ambiguity-float case. In ambiguity-fixed case, the average formal standard deviations are about 3–4 mm and 8 mm in the horizontal and vertical directions, respectively. In India, the averaged ambiguity-float standard

deviations amount to about 3–4 dm and 9 dm in the horizontal and vertical directions, and those in ambiguity-fixed case amount to about 2–4 mm and 5 mm in horizontal and vertical directions, respectively. In Japan, which is not shown in Fig. 11, the values in ambiguity-float case increase to about 1 and 2 m in the horizontal and vertical directions, and the ambiguity-fixed values are about 5–6 mm and 1 cm in the horizontal and vertical directions.

Baseline CUCC-UWA0

For the 8 km baseline CUCC–UWA0, multipath-mitigated solutions without and with the estimation of the between-receiver ZTDs are presented for DOY 103, 2018. The data on DOY 104, 2018 was used for multipath mitigation. Like with the short baseline CUT3–CUBB, only the time epochs with observations from 4 QZSS and 5 IRNSS satellites (I02, I03, I04, I05, I07) were used for the processing. The results are shown and discussed in the QZSS/IRNSS-combined case. Note that the processing time that we use does not show large DD ionospheric delays.

Figure 12 illustrates the north, east and height baseline errors of the single-epoch solutions without and with the estimation of the between-receiver ZTDs. It can be observed that estimating the between-receiver ZTDs leads to increasing errors mainly in the vertical direction. This is caused by the high correlation between the ZTDs and the kinematic height estimates (Rothacher and Beutler 1998). In the right

panel of Fig. 12, more wrongly-fixed ambiguities can be observed in the first half of the processing time. This corresponds to the higher ADOPs during this time span, which are illustrated with the black line.

From Fig. 12, between 2×10^4 and 2.3×10^4 s, increasing height errors can be observed when the between-receiver ZTDs are estimated. Extended from Zaminpardaz et al. (2018), for the single-epoch multi-system case, the baseline variance–covariance matrix with the estimation of the between-receiver ZTDs can be formulated as:

$$Q_{\hat{x}\hat{x}} = \begin{pmatrix} Q_{\hat{c}\hat{c}} & Q_{\hat{c}\hat{\tau}} \\ Q_{\hat{c}\hat{\tau}}^T & Q_{\hat{\tau}\hat{\tau}} \end{pmatrix} = \begin{pmatrix} N_{\hat{c}\hat{c}} & N_{\hat{c}\hat{\tau}} \\ N_{\hat{c}\hat{\tau}}^T & N_{\hat{\tau}\hat{\tau}} \end{pmatrix}^{-1} \tag{12}$$

$$= \left(\sum_{s=1}^m q^s (\beta^s - \bar{\beta})(\beta^s - \bar{\beta})^T \right)^{-1}$$

with

$$q^s = (\sigma_p^s)^{-2} \left((w_1^s)^{-1} + (w_2^s)^{-1} \right)^{-1} \tag{13}$$

$$\bar{\beta} = \frac{\sum_{s=1}^m (q^s \beta^s)}{\sum_{s=1}^m q^s} \tag{14}$$

where σ_p^s represents the zenith-referenced L5 code standard deviations of the corresponding system for satellite s . The subscript c and τ corresponds to the baseline elements

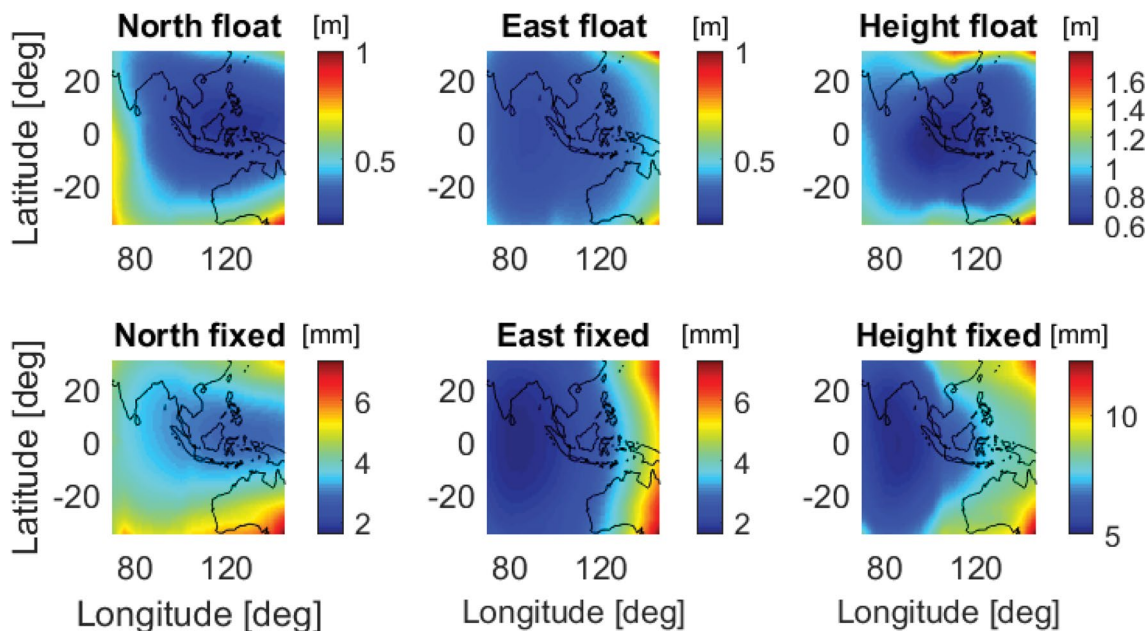


Fig. 11 Average formal standard deviations of the baseline errors. The processing was performed for L5 QZSS/IRNSS-combined case on DOY 77, 2018 using multipath-mitigated signal standard devia-

tions (Table 3). The epochs with less than 4 satellites or with PDOP larger than 100 were excluded from the analysis

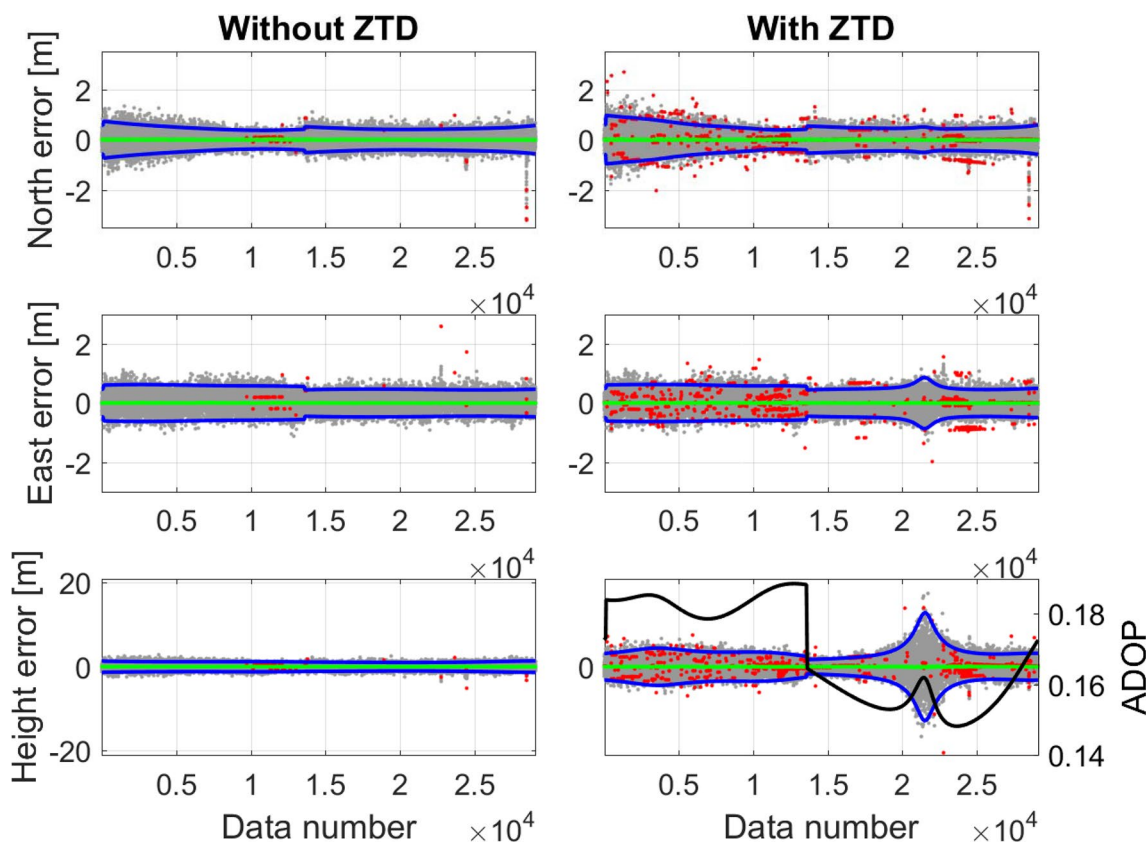


Fig. 12 Single-epoch north, east and height errors of the baseline CUCC–UWA0. The gray, green and red dots represent the ambiguity–float, ambiguity–correctly–fixed and ambiguity–wrongly–fixed solutions, respectively, without (left) and with the estimation of the between–receiver ZTDs (right). The black line illustrates the ADOPs with the between–receiver ZTDs estimated, and the blue lines repre–

sent the 95% formal confidence intervals of the float solutions. The processing is based on multipath–mitigated QZSS/IRNSS–combined L5 observations at the time points with observations available from 4 QZSS and 5 IRNSS (I02, I03, I04, I05, I07) on DOY 103 and 104 (shifted by 4 min for multipath mitigation), 2018

and the between–receiver ZTDs, respectively. The vector β^s is equal to $[(u^s)^T, g^s]^T$. The baseline variance–covariance matrix $Q_{\hat{c}\hat{c}}$ in this case can be formulated as:

$$Q_{\hat{c}\hat{c}} = N_{\hat{c}\hat{c}}^{-1} + \Delta Q \tag{15}$$

with

$$\Delta Q = N_{\hat{c}\hat{c}}^{-1} N_{\hat{c}\hat{t}} q N_{\hat{t}\hat{t}}^{-1} N_{\hat{c}\hat{c}}^{-1} \tag{16}$$

$$q = (N_{\hat{t}\hat{t}} - N_{\hat{c}\hat{t}}^T N_{\hat{c}\hat{c}}^{-1} N_{\hat{c}\hat{t}})^{-1} \tag{17}$$

where $N_{\hat{c}\hat{c}}^{-1}$ corresponds to the baseline variance–covariance matrix without estimation of the between–receiver ZTDs, and the term $(N_{\hat{t}\hat{t}} - N_{\hat{c}\hat{t}}^T N_{\hat{c}\hat{c}}^{-1} N_{\hat{c}\hat{t}})^{-1}$ is a scale that changes with the time, denoted by q . To explain the baseline precision differences without and with the estimation of the between–receiver ZTDs, the values of \sqrt{q} and $\sqrt{\text{diag}(\Delta Q)}$ (see 16) for the north, east and height components are shown in Fig. 13. Here $\text{diag}(\cdot)$ means the diagonal elements of the

matrix contained in (\cdot) . The change of \sqrt{q} almost only influences the height component of $\sqrt{\text{diag}(\Delta Q)}$, and the pattern corresponds to the change in the height errors, as shown in the right bottom panel of Fig. 12.

The empirical and formal standard deviations of the baseline errors and the ASRs are listed in Tables 8 and 9. Both the empirical and formal ASRs decrease by about 15% when the between–receiver ZTDs are estimated. With the ambiguities correctly fixed, standard deviations at mm– and cm–level can be obtained in the horizontal and vertical directions, respectively (Table 8). The ASRs are above 99% without the estimation of the between–receiver ZTDs.

For the 8 km baseline CUCC–UWA0, multi–epoch solutions were also computed using the same time epochs as in Fig. 12, i.e., the time points observing 4 QZSS and 5 IRNSS satellites. The ambiguities were assumed to be constant. The starting time of the processing was shifted by 1 epoch for each round of the processing. Only processing intervals

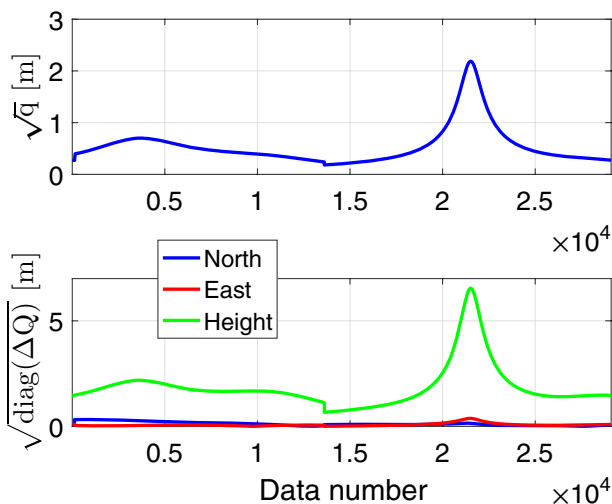


Fig. 13 Values of \sqrt{q} (top) and $\sqrt{\text{diag}(\Delta Q)}$ (bottom) (see 15). The day pair DOY 103/104 were used for computing the values in multipath-mitigated case

with continuous time epochs were used for the calculation. To reduce the influences of the remaining multipath on the dynamic model, the elevation mask was increased to 15°. The empirical and average formal ASRs of all processing rounds are listed in Table 10 for t of 2, 6 and 10 s. Without estimating the between-receiver ZTDs, the empirical and average formal ASRs already reach about 100% in 2 s. With the between-receiver ZTDs estimated, after 10 s, the empirical and average formal ASRs are about 99% and 100%, respectively. In our tested case, the case without estimating ZTDs shows better ambiguity resolution performance in both single- and multi-epoch cases. However, we remark that this may not necessarily apply for environments or time periods with strong DD ZTDs.

Conclusions

Taking advantage of the location of Australia, we evaluated the L5 single-epoch RTK performance from the two regional navigation satellite systems, QZSS and IRNSS. Using 1 Hz

Table 8 Empirical and average formal standard deviations of the single-epoch baseline errors

System	Direction	Ambiguity float (m)		Ambiguity-fixed (m)	
		Without ZTD	With ZTD	Without ZTD	With ZTD
QZSS/IRNSS	North	0.27 (0.24)	0.30 (0.28)	0.006 (0.007)	0.006 (0.007)
	East	0.26 (0.27)	0.28 (0.29)	0.005 (0.005)	0.005 (0.006)
	Height	0.63 (0.59)	1.93 (2.21)	0.013 (0.015)	0.034 (0.048)

The results are presented for the baseline CUCC-UWA0 with the formal results contained in brackets. The same time points on DOY 103, 2018 were used as in Fig. 12. Data on DOY 104, 2018 was used for multipath mitigation

Table 9 Single-epoch empirical and average formal ASRs (cf. 9, 11)

	Empirical ASR	Formal ASR
Without ZTD	0.995	0.991
With ZTD	0.847	0.829

The same time points on DOY 103, 2018 were used as in Fig. 12. Data on DOY 104, 2018 was used for multipath mitigation

L5-data simultaneously observed from 4 QZSS satellites and 5 IRNSS satellites (I02, I03, I04, I05, I07) above the elevation mask of 10°, for a very short baseline of 4 m, the QZSS/IRNSS-combined results were compared with the QZSS- and IRNSS-standalone solutions. In addition to that, the QZSS/IRNSS-combined results were also evaluated for an 8 km baseline without and with the between-receiver ZTDs considered in the observation model.

For the 4 m baseline, the single-epoch results show that the ASRs were significantly improved after combining both systems, i.e., from below 10% in standalone cases to almost 100% in the combined case. The standard deviations of the ambiguity-float positioning errors are reduced from meters to decimeters due to the much better geometry provided by both systems. After fixing the ambiguities, millimeter-level standard deviations can be obtained when using QZSS/IRNSS-combined observations. For this 4 m baseline in Perth, a formal analysis was also performed for the entire day with the GPS Block IIF satellites considered. It was found that the daily mean ASRs are below 30% for single-epoch single-system solutions using L5 signals. Combining any two systems of QZSS, IRNSS and GPS, or combining all three systems, lead to daily mean ASRs above 85% and millimeter-level positioning precision in ambiguity-fixed case. Based on the formal analysis performed for the short-baseline QZSS/IRNSS-combined solutions in a larger area, average formal standard deviations of the ambiguity-fixed positioning errors amount to about 3–4 and 8 mm in the horizontal and vertical directions, respectively, in the north-west of Australia.

For the 8 km baseline, the single-epoch solutions were processed in multipath-mitigated QZSS/IRNSS-combined case. We notice that estimating the between-receiver ZTDs increases the height errors due to the high correlation

Table 10 Multi-epoch empirical and average formal mean ASRs for baseline CUCC–UWA0 without and with the estimation of the between-receiver ZTDs

	Empirical ASR			Formal ASR		
	2 s	6 s	10 s	2 s	6 s	10 s
Without ZTD	1.000	1.000	1.000	1.000	1.000	1.000
With ZTD	0.975	0.988	0.990	0.989	1.000	1.000

The same time points on DOY 103, 2018 were used as in Fig. 12. Data on DOY 104, 2018 was used for multipath mitigation

between the ZTDs and the height estimates. In general, without large DD ionospheric delays observed in the processing time, standard deviations of the ambiguity-fixed positioning errors can be obtained at millimeter- and centimeter-level in horizontal and vertical directions, respectively. For single-epoch solutions, the ASRs are above 80% and 99% with and without the estimation of the between-receiver ZTDs, respectively. For multi-epoch solutions with a higher elevation mask of 15°, at a processing time of 10 s, the empirical ASRs are about 99% and 100%, respectively, with and without the estimation of the between-receiver ZTDs.

Acknowledgements We would like to thank Septentrio for providing the receiver at station UWA0 and Dr. Sascha Schediwy from the University of Western Australia for hosting this station. Thanks are also given to IGS MGEX and CDDIS for providing the combined broadcast ephemeris on the server. Peter J.G. Teunissen is the recipient of an Australian Research Council (ARC) Federation Fellowship (Project Number FF0883188). The work of Pei Chen is funded in part by Ministry of Science and Technology of China through cooperative agreement No. 2014CB845303.

References

- Amiri-Simkooei AR, Teunissen PJG, Tiberius CCJM (2009) Application of least-squares variance component estimation to GPS observables. *J Surv Eng* 135(4):149–160. [https://doi.org/10.1061/\(ASCE\)0733-9453\(2009\)135:4\(149\)](https://doi.org/10.1061/(ASCE)0733-9453(2009)135:4(149))
- BRDM (2018) Combined MGEX broadcast ephemeris files. <ftp://ftp.cddis.eosdis.nasa.gov/gnss/data/campaign/mgex/daily/rinex/3/2018/brdm>
- Euler HJ, Goad CC (1991) On optimal filtering of GPS dual frequency observations without using orbit information. *Bull Geod* 65(2):130–143. <https://doi.org/10.1007/BF00806368>
- Google Earth (2018) Google Earth imagery (November 5, 2017). Google Earth 7.0.3.8542. Perth, Australia. 31 deg 59 min 21.91 sec (S), 115 deg 51 min 30.35 sec (E), Eye alt 8.3 km. @ 2018 Google. <https://www.google.com/earth/>. Accessed 30 Apr 2018
- Hauschild A, Steigenberger P, Rodríguez-Solano C (2012) Signal, orbit and attitude analysis of Japan's first QZSS satellite Michibiki. *GPS Solut* 16(1):127–133. <https://doi.org/10.1007/s10291-011-0245-5>
- Ifadis II (1986) The atmospheric delay of radio waves: modeling the elevation dependence on a global scale. Technical Report 38L, Chalmers University of Technology, Göteborg, Sweden
- ISRO (2018) List of Navigation Satellites. Department of Space, Indian Space Research Organisation. <https://www.isro.gov.in/spacecraft/list-of-navigation-satellites>. Accessed Apr 2018
- MGEX (2017a) QZSS. IGS, MGEX. http://mgex.igs.org/IGS_MGEX_Status_QZSS.php
- MGEX (2017b) NAVIC. IGS, MGEX. http://mgex.igs.org/IGS_MGEX_Status_IRNS.php
- Montenbruck O, Steigenberger P, Prange L, Deng Z, Zhao Q, Perosanz F, Romero I, Noll C, Stürze A, Weber G, Schmid R, MacLeod K, Schaer S (2017) The multi-GNSS experiment (MGEX) of the International GNSS Service (IGS)—Achievements, prospects and challenges. *Adv Space Res* 59(7):1671–1697. <https://doi.org/10.1016/j.asr.2017.01.011>
- Nadarajah N, Khodabandeh A, Teunissen PJG (2016) Assessing the IRNSS L5-signal in combination with GPS, Galileo, and QZSS L5/E5a-signals for positioning and navigation. *GPS Solut* 20(2):289–297. <https://doi.org/10.1007/s10291-015-0450-8>
- Nie X, Zheng F, Lou Y, Zheng J, Li Z (2015) An analysis of the QZSS signal based on the data of IGS. In: Sun J et al (eds) China satellite navigation conference (CSNC) 2015. Proceedings: volume II, Lecture notes in electrical engineering, vol 341. https://doi.org/10.1007/978-3-662-46635-3_27
- NSPS (2018a) Start of QZS-4 Trial Service. Cabinet Office, National Space Policy Secretariat. http://qzss.go.jp/en/overview/notices/trial-qzs4_180112.html
- NSPS (2018b) Overview of the Quasi-Zenith Satellite System (QZSS). Cabinet Office, National Space Policy Secretariat. http://qzss.go.jp/en/overview/services/sv01_what.html
- Odijk D, Teunissen PJG (2008) ADOP in closed form for a hierarchy of multi-frequency single-baseline GNSS models. *J Geodesy* 82:473–492. <https://doi.org/10.1007/s00190-007-0197-2>
- Odijk D, Nadarajah N, Zaminpardaz S, Teunissen PJG (2017) GPS, Galileo, QZSS and IRNSS differential ISBs: estimation and application. *GPS Solut* 21(2):439–450. <https://doi.org/10.1007/s10291-016-0536-y>
- Odolinski R, Teunissen PJG (2017) Low-cost, 4-system, precise GNSS positioning: a GPS, Galileo, BDS and QZSS ionosphere-weighted RTK analysis. *Meas Sci Technol* 28(12):125801. <https://doi.org/10.1088/1361-6501/aa92eb>
- Odolinski R, Teunissen PJG, Odijk D (2015) Combined BDS, Galileo, QZSS and GPS single-frequency RTK. *GPS Solut* 19(1):151–163. <https://doi.org/10.1007/s10291-014-0376-6>
- Rothacher M, Beutler G (1998) The role of GPS in the study of global change. *Phys Chem Earth* 23(9–10):1029–1040. [https://doi.org/10.1016/S0079-1946\(98\)00143-8](https://doi.org/10.1016/S0079-1946(98)00143-8)
- Saastamoinen J (1972) Atmospheric correction for troposphere and stratosphere in radio ranging of satellites. In: Henriksen SW, Mancini A, Chovitz BH (eds) The use of artificial satellites for geodesy, Geophysics Monograph Series, vol 15. American Geophysical Union, Washington, DC, pp 247–251
- Teunissen PJG (1997) A canonical theory for short GPS baselines. Part IV: precision versus reliability. *J Geodesy* 71(5):513–525. <https://doi.org/10.1007/s001900050119>
- Teunissen PJG (1998) Success probability of integer GPS ambiguity rounding and bootstrapping. *J Geodesy* 72(10):606–612. <https://doi.org/10.1007/s001900050199>

- Teunissen PJG (1999) An optimality property of the integer least-squares estimator. *J Geodesy* 73(11):587–593. <https://doi.org/10.1007/s001900050269>
- Teunissen PJG, Amiri-Simkooei AR (2008) Least-squares variance component estimation. *J Geodesy* 82(2):65–82. <https://doi.org/10.1007/s00190-007-0157-x>
- Teunissen PJG, Montenbruck O (eds) (2017) Springer handbook of global navigation satellite systems. Springer International Publishing, Cham. <https://doi.org/10.1007/978-3-319-42928-1>
- Zaminpardaz S, Teunissen PJG, Nadarajah N (2016) IRNSS stand-alone positioning: first results in Australia. *J Spat Sci* 61(1):5–27. <https://doi.org/10.1080/14498596.2016.1142398>
- Zaminpardaz S, Teunissen PJG, Nadarajah N (2017) IRNSS/NavIC and GPS: a single- and dual-system L5 analysis. *J Geodesy* 91(8):915–931. <https://doi.org/10.1007/s00190-016-0996-4>
- Zaminpardaz S, Wang K, Teunissen PJG (2018) Australia-first high-precision positioning results with new Japanese QZSS regional satellite system. *GPS Solut* 22:101. <https://doi.org/10.1007/s10291-018-0763-5>



Safoora Zaminpardaz received her Ph.D. in Geodesy and GNSS from Curtin University in 2018. She is now a lecturer in Geospatial Sciences at RMIT University, Melbourne, Australia. Her research interests include array-based multi-GNSS positioning, integrity monitoring and ionosphere sensing.



Peter J. G. Teunissen is Professor of Geodesy and Navigation at the Delft University of Technology, Delft, The Netherlands, and Curtin University, Perth, Australia. He is the recipient of an Australian Research Council (ARC) Federation Fellowship (project number FF0883188). His current research interests are multi-GNSS and multi-frequency precise positioning, navigation and timing applications.



Kan Wang is a research associate in Department of Spatial Sciences, Curtin University. She received her PhD in GNSS advanced modeling from ETH Zurich in 2016, and works on SBAS, satellite clock modeling, multi-frequency and multi-GNSS ambiguity resolution and PPP-RTK processing.



Pei Chen received his Ph.D. degree in aerospace engineering from Beihang University, Beijing, in 2007. He is currently an associate professor at the School of Astronautics, Beihang University. His current research activities comprise spacecraft navigation, GNSS application, and orbit determination.